Check for updates

JGR Space Physics

RESEARCH ARTICLE
10.1029/2021JA029910

Conductivities of Titan's Dusty Ionosphere

O. Shebanits[1], J.-E. Wahlund[1], J. H. Waite[2], and M. K. Dougherty[3]

[1]Swedish Institute of Space Physics, Uppsala, Sweden, [2]Southwest Research Institute, San Antonio, TX, USA, [3]Imperial College London, London, UK

Key Points:

- Titan's ionospheric conductivities from in-situ measurements with full plasma content (electrons, pos. ions, neg. ions/dust grains)
- Indications of reverse Hall effect near ~900 km altitude
- Most impact of dusty plasma at ~1,100–1,200 km altitude—up to 35% increase for Pedersen conductivities

Correspondence to:

O. Shebanits,
oleg.shebanits@irfu.se

Citation:

Shebanits, O., Wahlund, J.-E., Waite, J. H., & Dougherty, M. K. (2022). Conductivities of Titan's dusty ionosphere. *Journal of Geophysical Research: Space Physics*, *127*, e2021JA029910. https://doi.org/10.1029/2021JA029910

Received 24 AUG 2021
Accepted 21 JAN 2022

Author Contributions:

Conceptualization: O. Shebanits
Data curation: O. Shebanits, J.-E. Wahlund, J. H. Waite, M. K. Dougherty
Formal analysis: O. Shebanits
Funding acquisition: O. Shebanits
Investigation: O. Shebanits
Methodology: O. Shebanits
Project Administration: O. Shebanits
Resources: O. Shebanits
Software: O. Shebanits
Supervision: O. Shebanits
Validation: O. Shebanits
Visualization: O. Shebanits
Writing – original draft: O. Shebanits
Writing – review & editing: O. Shebanits, J.-E. Wahlund, J. H. Waite, M. K. Dougherty

© 2022 The Authors.
This is an open access article under the terms of the Creative Commons Attribution-NonCommercial License, which permits use, distribution and reproduction in any medium, provided the original work is properly cited and is not used for commercial purposes.

Abstract Titan's ionosphere hosts a globally distributed non-trivial dusty ion-ion plasma, providing an environment for studies of dusty ionospheres that is in many aspects unique in our solar system. Thanks to the Cassini mission, Titan's ionosphere also features one of the largest dusty plasma data sets from 126 flybys of the moon over 13 years, from 2004 to 2017. Recent studies have shown that negatively charged dust dramatically alters the electric properties of plasmas, in particular planetary ionospheres. Utilizing the full plasma content of the moon's ionosphere (electrons, positive ions, and negative ions/dust grains), we derive the electric conductivities and define the conductive dynamo region. Our results show that using the full plasma content increases the Pedersen conductivities at ~1,100–1,200 km altitude by up to 35% compared to the estimates using only electron densities. The Hall conductivities are in general not affected but several cases indicate a reverse Hall effect at ~900 km altitude (closest approach) and below. The dayside conductivities are shown to be factor ~7–9 larger than on the nightside, owing to higher dayside plasma densities.

Plain Language Summary Titan (largest moon of Saturn) is famous for its signature orange haze, formed in the top layer of its atmosphere–ionosphere. The complex organic chemistry initiated mainly by sunlight forms grains of dust that at ~1,000 km altitude reach a few nanometers in size (comparable to finely ground flour). In the ionosphere, these grains of dust absorb the free electrons (depleting them) and become charged. Below ~1,000 km altitude there is very little electrons and the plasma consists primarily of ions–called "ion-ion" or "dusty" plasma. In the absence of light electrons (negative charge), the positively charged ions instead become the dominant mobile charge carrier, as the negatively charged dust is much heavier. Such a reversal of charge mobility has a large impact on the electric properties of an ionosphere, increasing its electric conductivity and changing the direction of its electric currents. We use a Cassini mission data set spanning an entire solar cycle, nearly half a Titan year (≈15 Earth years), to calculate the electric conductivities of Titan's ionosphere and show that dusty plasma typically contributes up to 35%. We also find indications of the charge mobility reversal below 1,000 km although it is not a persistent feature.

1. Introduction

Titan is immersed in Saturn's magnetosphere (Bertucci et al., 2008; Garnier et al., 2010) and does not have its own magnetic field. Instead, an induced magnetic field is formed around Titan from the interactions with Saturn's magnetosphere (Wahlund et al., 2005), similarly to interactions of Venus and Mars with the solar wind and interplanetary magnetic field (e.g., Bertucci et al., 2011 and references therein). The interaction between Titan and the ambient magnetic field depends to a large degree on Titan's conductive ionosphere. Previously, the electrical properties of Titan's ionosphere were derived using only the ion and electron content (Rosenqvist et al., 2009). In the later years, the data sets have been significantly updated. Most notably, large amounts of charged dust were detected in Titan's ionosphere (Ågren et al., 2012; Coates et al., 2007; Shebanits et al., 2013) and a globally present dusty ion-ion plasma is expected (Shebanits et al., 2016). The charged dust grains in the ionosphere-like plasma of Enceladus plume (Morooka et al., 2011) and in the near-equatorial dusty ionosphere of Saturn (Morooka et al., 2019) were shown to have a profound effect on its electric conductivities by Simon et al. (2011) and Yaroshenko and Lühr (2016), and Shebanits et al. (2020), respectively. In this work we derive the electrical properties of Titan's ionosphere using the full plasma content: electrons, positive ions and negative ions/dust grains and investigate the impact of dusty plasma on an unmagnetized planetary body. The relevant in-situ measurements used here are from the Radio and Plasma Wave Science Langmuir Probe (RPWS/LP, Gurnett et al., 2004), the Ion and Neutral Mass Spectrometer (INMS, Teolis et al., 2015; Waite et al., 2004) and the Cassini Fluxgate Magnetometer (MAG, Dougherty et al., 2004). The data set spans the entire Cassini mission and is representative of a full solar cycle and nearly half Titan year.

2. Observations and Method

2.1. Datasets and Flyby Coverage

We use data from 58 flybys where measurements of the Cassini INMS, RPWS/LP and the Cassini MAG are simultaneously available at the altitudes below 1,600 km down to the closest approach (CA) of 950 km (**T#:** A, B, 5, 16–21, 23, 25–30, 32, 34, 36, 38–40, 42–44, 46, 48–51, 55–59, 61, 65, 71, 77, 83, 84, 86, 87, 91, 92, 95, 98, 100, 104, 107, 108, 113, and 116–121). The primary data from the INMS are the N_2 and CH_4 densities. The Cassini RPWS/LP data set provides electron temperatures (Ågren et al., 2009) and electron densities, positive ion densities, negative ion densities, derived as described in Shebanits et al. (2016) with photoelectron current correction updated to account for the Cassini shadow over RPWS/LP (affects 15 flybys, T#: A, 21, 27, 44, 49, 91, 92, 95, 98, 100, 105, 108, 119, 120, and 121). The INMS ion data are used as supplementary for the ion mass information in the RPWS/LP analysis (Shebanits et al., 2016). The Cassini MAG provides the *in-situ* magnetic field strength measurements. Regarding the RPWS/LP derived electron density and temperature, Chatain et al. (2021a, 2021b) provides a very detailed analysis of the electron current, showing that in Titan's ionosphere it consists of up to three electron populations as well as secondary electrons emitted from the s/c. However, the main populations have similar properties and their net densities and temperatures are consistent with the earlier estimates of the bulk temperatures and densities by Ågren et al. (2009) and Edberg et al. (2010, 2013a, 2018). Due to the complexity of the analysis, dividing the electrons into three polulations also introduces significant error margins (Chatain et al., 2021a). Another way to estimate the bulk electron density is by means of quasineutrality using the ram ion current as detailed in Shebanits et al., 2016. The ram ion current is by definition independent of the ion and dust masses. Because of the high velocity of the Cassini s/c in Titan's ionosphere (~6 km/s), the ram ion current is also virtually undisturbed by the thermal component, offering a very robust estimate of the bulk electron density with a standard deviation of <90 cm^{-3}, accounting for neutral winds up to ~300 m/s (Lellouch et al., 2019), measurement noise, and a conservative 0.1 V uncertainty in the measured spacecraft potential. For the calculation of conductivities we therefore estimate the ionospheric electron density from the net ion current and use the bulk electron temperature from the electron current.

2.2. Method

2.2.1. Conductivities

The ionospheric conductivity tensor is traditionally separated into an orthogonal set with respect to the background magnetic field, stemming from the mathematical derivation of the ionospheric current from the momentum equation dominated by the Lorentz force (e.g., Schunk & Nagy, 2009). As such, the direction of the Pedersen conductivity (σ_P) is defined as orthogonal to the magnetic field $\boldsymbol{B}$ and parallel to the electric field $\boldsymbol{E}_\perp$ (driving the Pedersen current), the direction of the Hall conductivity (σ_H) is defined as orthogonal to the magnetic and electric fields (anti-parallel to the $\boldsymbol{E}\times\boldsymbol{B}$ drift) and the parallel conductivity ($\sigma_\parallel$, $\parallel\boldsymbol{B}$) completes the set. Using the conductivity tensor representation (Schunk & Nagy, 2009) with dust term added (Shebanits et al., 2020; Simon et al., 2011; Yaroshenko & Lühr, 2016), the Pedersen (σ_P), Hall (σ_H) and magnetic field parallel ($\sigma_\parallel$) conductivities are defined as:

$$\begin{aligned}\sigma_P &= \sum_{s=e,i,d} n_s \frac{q_s}{B}\frac{\nu_s\Omega_s}{\nu_s^2+\Omega_s^2}\\ \sigma_H &= -\sum_{s=e,i,d} n_s \frac{q_s}{B}\frac{\Omega_s^2}{\nu_s^2+\Omega_s^2}\\ \sigma_\parallel &= \sum_{s=e,i,d} \frac{n_s q_s^2}{m_s \nu_s}\end{aligned} \tag{1}$$

Here, the subscripts (s) denotes electrons (e), positive ions (i) and negative ions/dust grains (d) and the input plasma parameters are number density (n), mass (m), charge (q), momentum transfer collision frequency (ν), gyrofrequency (Ω), and magnetic field strength (B). Note that the gyrofrequency $\Omega = q_s B/m_s$ has the same sign as q_s.

Strictly speaking, the equations for conductivities must be summed over all the plasma species. However, mass spectra information is of very limited availability for Titan's ionosphere. We therefore adopt the average masses for the positive ions and for the negative ions/dust grains as described in Shebanits et al. (2016). Additionally,

singly charged negative ions/dust grains are assumed. This approach is validated using several flybys where the mass spectra for the positive ions and the negative ions and dust grains are available simultaneously (Coates et al., 2009; Shebanits et al., 2016), see Appendix A.

2.2.2. Momentum Transfer Collision Frequencies

In the following equations, the number density is always in cm^{-3}, the rest of the units are SI. It should be noted that since the RPWS/LP measures the total charged particle flux at a given bias voltage and the availability of the mass spectra is limited, we use the total charge densities for the positive ions and negative ions/dust grains together with their respective mean mass as derived and validated in Shebanits et al. (2016). The collision frequencies (and in turn, conductivities) therefore represent mass-averages as well.

The momentum transfer collision frequencies (MTCFs) are largely dominated by collisions with neutrals. However, in a dusty plasma a significant contribution from collisions with the negative ions/dust grains is present and cannot be discarded (Shebanits et al., 2020; Yaroshenko & Lühr, 2016). We therefore use the total momentum transfer collision frequencies (MTCF) for each species as a sum of collision frequencies with the other species:

$$\nu_{s,\mathrm{tot}} = \sum_{t \neq s} \nu_{\mathrm{st}}$$

The main neutral species in Titan's atmosphere are N_2 and CH_4 (Niemann et al., 2005; Waite et al., 2005). Collisions of electrons with N_2 and CH_4 are implemented as hard-sphere collisions (e.g., Schunk & Nagy, 2009) with the appropriate electron temperature dependent cross-sections $\chi(T_e)$ for N_2 (Itikawa, 2006) and CH_4 (Song et al., 2015):

$$\nu_{e-\mathrm{neutral}} = n_{\mathrm{neutral}} \frac{8}{3} \sqrt{\frac{2k_b T_e}{\pi m_e}} \chi_{\mathrm{neutral}}(T_e) \tag{2}$$

For the negative ion/dust collisions with neutrals, both elastic (Coulomb) and hard-sphere collisions are used (see also Shebanits et al., 2020). For the hard-sphere collisions, the cross-sections are replaced by the average dust grain cross-section πR_d^2, where the average dust grain radius R_d is estimated from the average grain mass by assuming a spherical grain and a mass density of kerogen (1280 ± 300 kgm^{-3}, Stankiewicz et al., 2015):

$$\nu_{d-\mathrm{neutral}} = \frac{8}{3\sqrt{\pi}} \frac{n_n m_n}{m_d + m_n} \sqrt{2k_b \frac{m_n T_d + m_d T_n}{m_n m_d}} \pi R_d^2 \tag{3}$$

The kerogen mass density is consistent with a range of tholin mass densities derived in lab settings (Imanaka et al., 2012) as well as comet 67P tholin analogs (Brouet et al., 2016). It should be noted that the actual dust grain geometry in Titan's ionosphere is likely to be of fractal nature (Chatain et al., 2020; Michael et al., 2011; Shebanits et al., 2016; Sittler et al., 2009; Waite et al., 2009). However, extensive lab experiments and sophisticated modeling are required to produce a database of dust grain geometries (and their cross-sections) at Titan. We therefore adapt spherical grains as a first order approximation.

Elastic collisions of electrons and neutrals with the heavy charged species are calculated according to Schunk and Nagy (2009), their equation 4.144 and 4.88, respectively:

$$\nu_{e-i,d} = 54.5 \frac{n_{i,d} Z_{i,d}^2}{T_e^{1.5}}, \tag{4}$$

$$\nu_{i,d-\mathrm{neutral}} = 2.5879 \times 10^{-9} n_n \sqrt{\frac{Y_n}{m_{i,d}} \frac{m_n}{m_n + m_{i,d}}}, \tag{5}$$

where, the charge number is defined as $Z_{i,d} = q_{i,d}/|q_e|$ and Y_n is the polarizability of the neutral molecule ($Y_{CH_4} = 2.59$, $Y_{N_2} = 1.76$).

MTCF equation for elastic collisions between the positive ions and negative ions/dust grains (ion-dust drag) is the same as ion-ion collision (equation 4.142 in Schunk & Nagy, 2009):

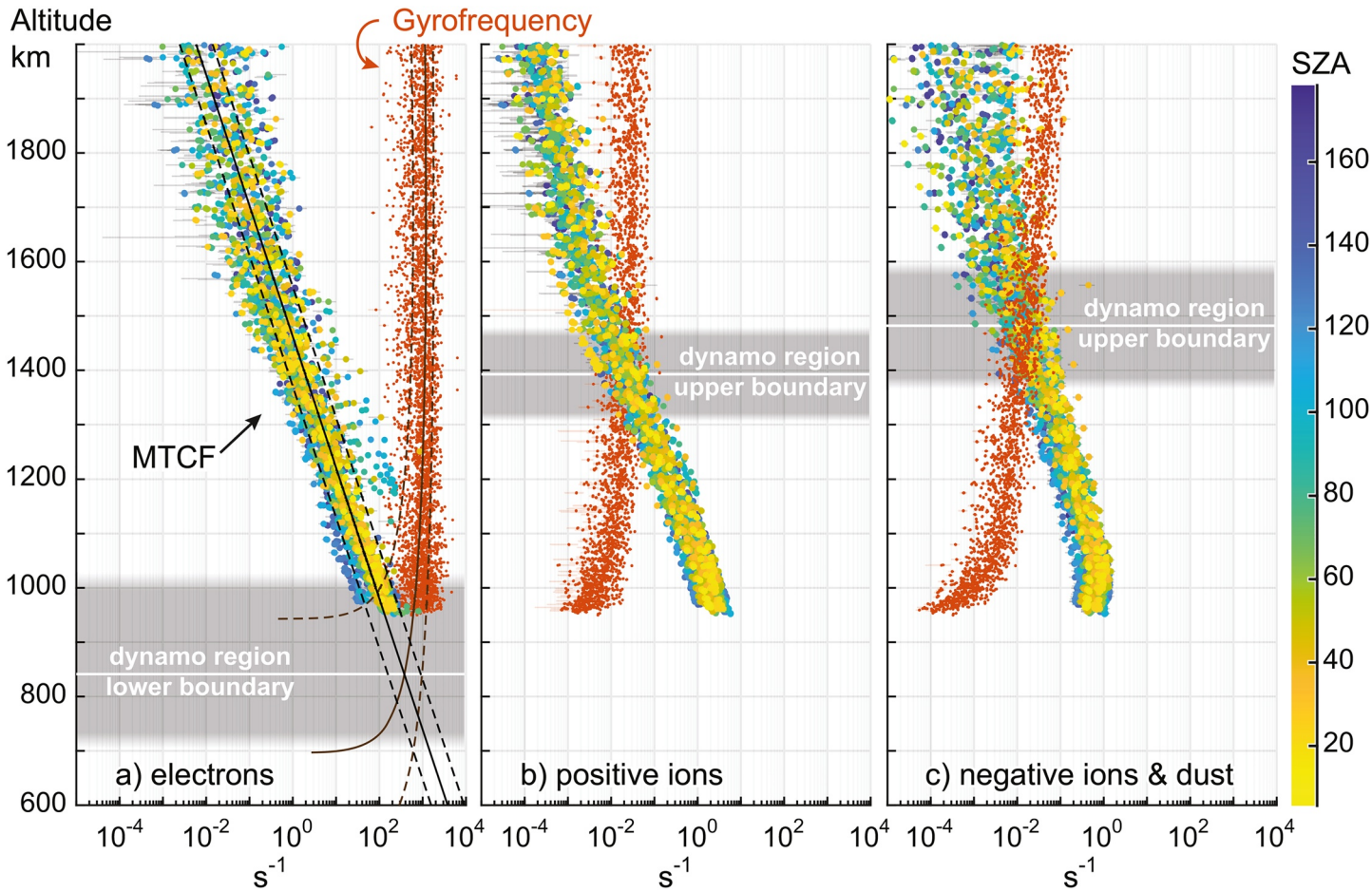

Figure 1. Momentum transfer collision frequencies (color-coded by solar zenith angle) and gyrofrequencies (orange) for electrons (panel a), positive ions (panel b) and negative ions/dust grains (panel c). The dynamo region boundary statistics from all included flybys: the mean values are shown as solid black lines and the corresponding standard deviations as dashed lines. For the lower boundary, the electron frequencies are extrapolated as defined in the text.

$$\nu_{\mathrm{id}} = 1.27 \; Z_d^2 Z_i^2 \frac{n_d}{m_i} (m_i + m_d) \sqrt{\frac{m_d m_i}{(m_i T_d + m_d T_i)^3}} \tag{6}$$

3. Results and Discussion

3.1. Dynamo Region

The conductive region of an ionosphere is called a dynamo region. It is a layer where the heavy charge carriers are coupled to the neutral atmosphere (i.e., gyrofrequency < MTCF, upper boundary) while the electrons can still move along the magnetic field lines (i.e., gyrofrequency > MTCF, lower boundary). The MTCFs and gyrofrequencies defining the dynamo region of Titan's ionosphere are shown in Figure 1, plotted in altitude with the solar zenith angle (SZA) colorcoded. The error bars are symmetric and represent the combined measurement uncertainty (2σ level), propagated from the individual measurement uncertainties using the Monte-Carlo method (10^5 iterations). The statistical means of the dynamo region boundaries from all included flybys are given in solid white lines, with standard deviations as shaded areas.

The top boundary of the positive ions is at 1390 ± 90 km, in agreement with previous estimates (Rosenqvist et al., 2009). The negative ions and dust grains begin to conduct at ~100 km higher altitudes due to their higher mass and subsequently lower gyrofrequency (see also Shebanits et al., 2020). However, since the negative ions and dust grains are nearly absent above 1,200 km altitude in Titan's ionosphere, their impact on the top boundary of the dynamo region is negligible.

It should be noted that the lower boundary defined by electrons (panel a) is a rough estimate derived empirically from an exponential extrapolation of the electron MTCFs (dominant trend from the neutral densities) and a linear extrapolation of their gyrofrequencies (i.e., magnetic field). The magnetic field is only available from the *in-situ* measurements which are limited by the closest approach, so a more sophisticated extrapolation is not deemed necessary for this work. In light of this, the lower boundary is constrained to be between 700 and 1,000 km altitude, with lower altitudes more likely in the nightside ionosphere as indicated by the SZA trend (blue end of the colorbar = nightside). Incidentally, the dusty plasma in Titan's ionosphere is expected to peak below 1,000 km (Shebanits et al., 2016).

The rather large variability in the top dynamo region boundary (Figure 1) is a combination of the variabilities in the background neutral densities, magnetic field, SZA and the local time. The scatter in the ion/dust gyrofrequency is mostly due to variations in the magnetic field, as evident when comparing to the spread in the electron gyrofrequency. The top dynamo boundary variability is illustrated in Figure 2, where the top boundaries for positive ions are plotted in the leftside panels a1, a2 and for negative ions and dust grains in the rightside panels b1, b2 (throughout the text, the panels in figures are labeled with letters for columns and numbers for rows, for easier referencing). The altitudes of top boundaries are determined by a $\nu_{i,d} = \Omega_{i,d}$ condition estimated at 1s resolution (linearly interpolated), resulting in ∼6 km error margin. The magnetic field strength $|B|$ is proportional to marker size and the local time is colorcoded. Solid black lines are moving medians (50-points sliding window, producing essentially a piece-wise linear fit).

The most obvious factor is $|B|$, with stronger field (larger markers) corresponding to lower altitudes (panels a1, b1) and higher neutral densities (panels a2, b2). The SZA dependency is noticeable for the negative ions and dust grains but is much weaker for the positive ions, propagated from their respective masses. Although for the negative ions the median is roughly linearly decreasing in altitude from dayside to nightside (panel b1), when plotted in the background neutral densities instead (panel b2) the decrease is only clear on the nightside, possibly due to cooling and contraction of the neutral atmosphere. There is a slight difference between dawn (blue) and dusk (orange) regions for the negative ions and dust grains (right side, panels b1–2). As a side note, this difference may be examined using appropriate statistical methods – the unpaired t-test (difference of means, assuming normal pdf and different variances) and the Wilcoxon rank sum test (difference of medians, no pdf assumed). In altitudes (panel b1) the t-test gives a p-value of 0.0923 and the rank sum test gives 0.0663 (weak evidence). In neutral densities however (panel b2), the p-values are 0.0152 and 0.0286 respectively, both of which are statistically sufficient evidence at 95% significance level for the dawn-dusk difference. The underlying reason for this difference is likely a difference in the masses of the negative ions and dust grains, with generally heavier particles present at dusk due to their continuous formation (e.g., Waite et al., 2007). While certainly interesting, this result has no consequences for the conductive dynamo region, since its top boundary is governed by the more numerous positive ions as mentioned above.

3.2. Conductivities

Titan's ionospheric conductivities are shown in Figure 3 versus altitude (left side, panels a1–a3) and measured N_2 densities (right side, panels b1–b3), color-coded with SZA. The error bars are symmetric and represent the combined uncertainties of measurements, collision cross-sections and masses of heavy plasma species (2σ level). The error bars are one-sided for points where the uncertainties reach zero (omitted on log scale to reduce clutter). The square markers in panels a2 and b2 mark negative values of σ_H. The empty markers in all panels show the data points with low signal-to-noise ratio (positive ion densities < 10 cm^{-3}). The field parallel conductivities $\sigma_\parallel$ separating into two profiles above ∼1,400 km altitude clearly demonstrate this, with the left profile (lower values) essentially showing the measurement limit of $\sigma_\parallel$ for that region.

The SZA trends for the ionospheric conductivities are inherited from the ionospheric plasma number densities, with σ_P and σ_H being approximately linearly proportional to the positive ion densities and $\sigma_\parallel$ to the electron densities.

Pedersen conductivities σ_P have a peak between 1,200 and 1,400 km altitude and increase sharply below 1,100 km. At altitudes of ∼1,400 km, $\sigma_H > \sigma_P$ and the Hall currents are the dominant horizontal currents (Ågren et al., 2011). However, at the CA the σ_H drops in the increasing presence of the dusty plasma. In a dusty plasma, σ_H is expected to reverse (reverse Hall effect) due to the electron depletion onto the dusty grains. Such cases have

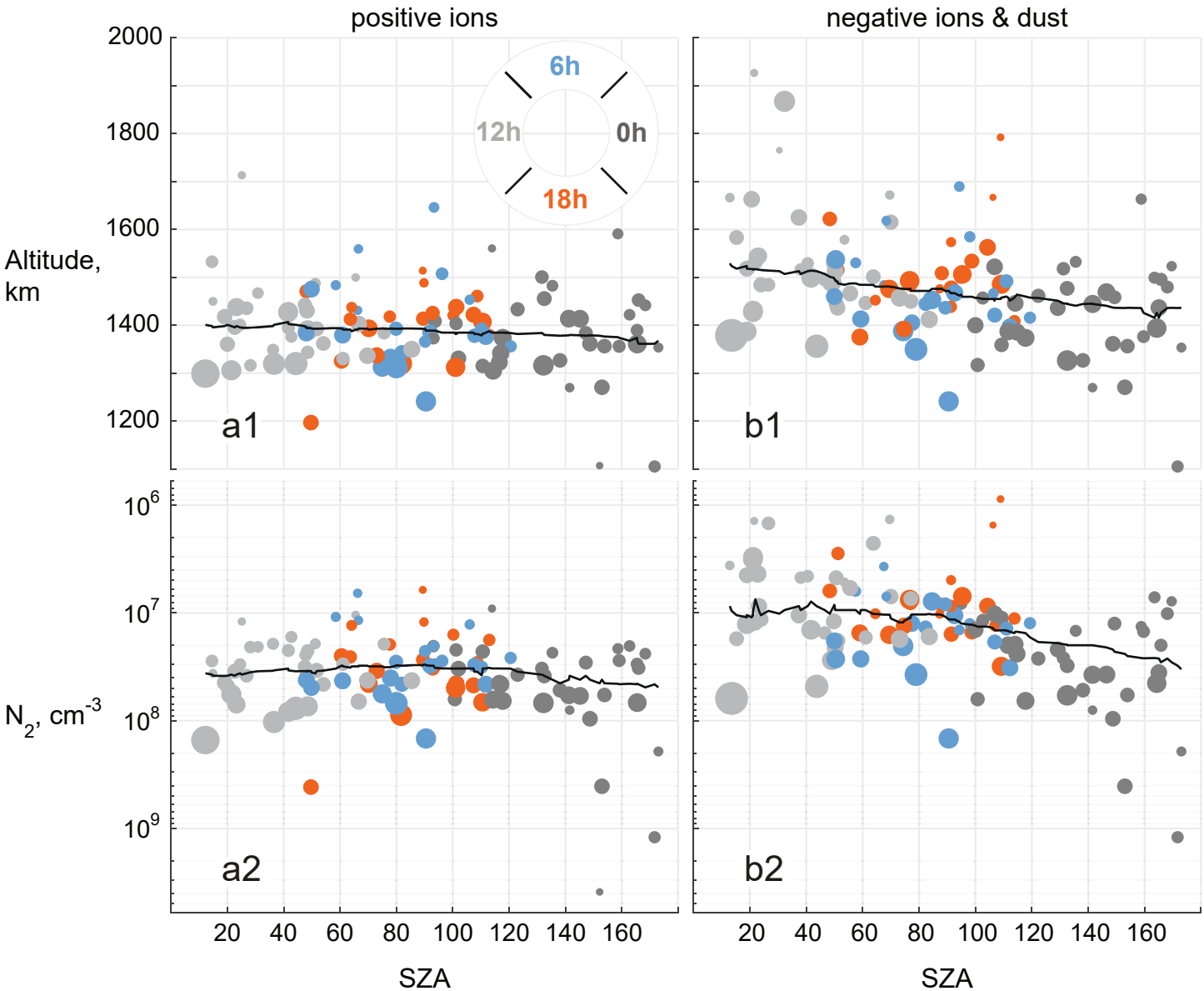

Figure 2. Dynamo region top boundaries statistics for positive ions (left side panels a1, a2) and for negative ions and dust grains (right side panels b1, b2), plotted in altitude (top panels a1, b1) and in the measured N_2 densites (bottom panels a2, b2) versus solar zenith angle . Size of markers is proportional to the magnetic field strength $|\boldsymbol{B}|$. Titan Local Time is color-coded.

been measured in Earth's E-region (Muralikrishna & Kulkarni, 2006) and near-equatorial ionosphere of Saturn (Shebanits et al., 2020). A reverse Hall effect also explains the anomalies in the Alfvén wing structure near the Enceladus plume (Simon et al., 2011; Yaroshenko & Lühr, 2016). The small cluster of data points marked with red arrows in Figure 3 panels a2, b2 is indicative of the σ_H reversal (square markers are $\sigma_H < 0$). With σ_H quenched or reversed and σ_P increasing below the CA, it is therefore possible that a secondary layer of Pedersen current exists when the bottom boundary of the dynamo region extends enough to include the dusty plasma region below 900 km altitude.

Such a configuration of ionospheric currents has not been observed before. While the second Pedersen layer has been proposed already in Rosenqvist et al., 2009, the effect of dusty plasma on this region has not been considered to date. The works cited above show that the dusty plasma in ionospheres of Earth, Saturn and plume of Enceladus significantly increases σ_P. In addition, the presence of dust is expected to enhance the bulk plasma densities

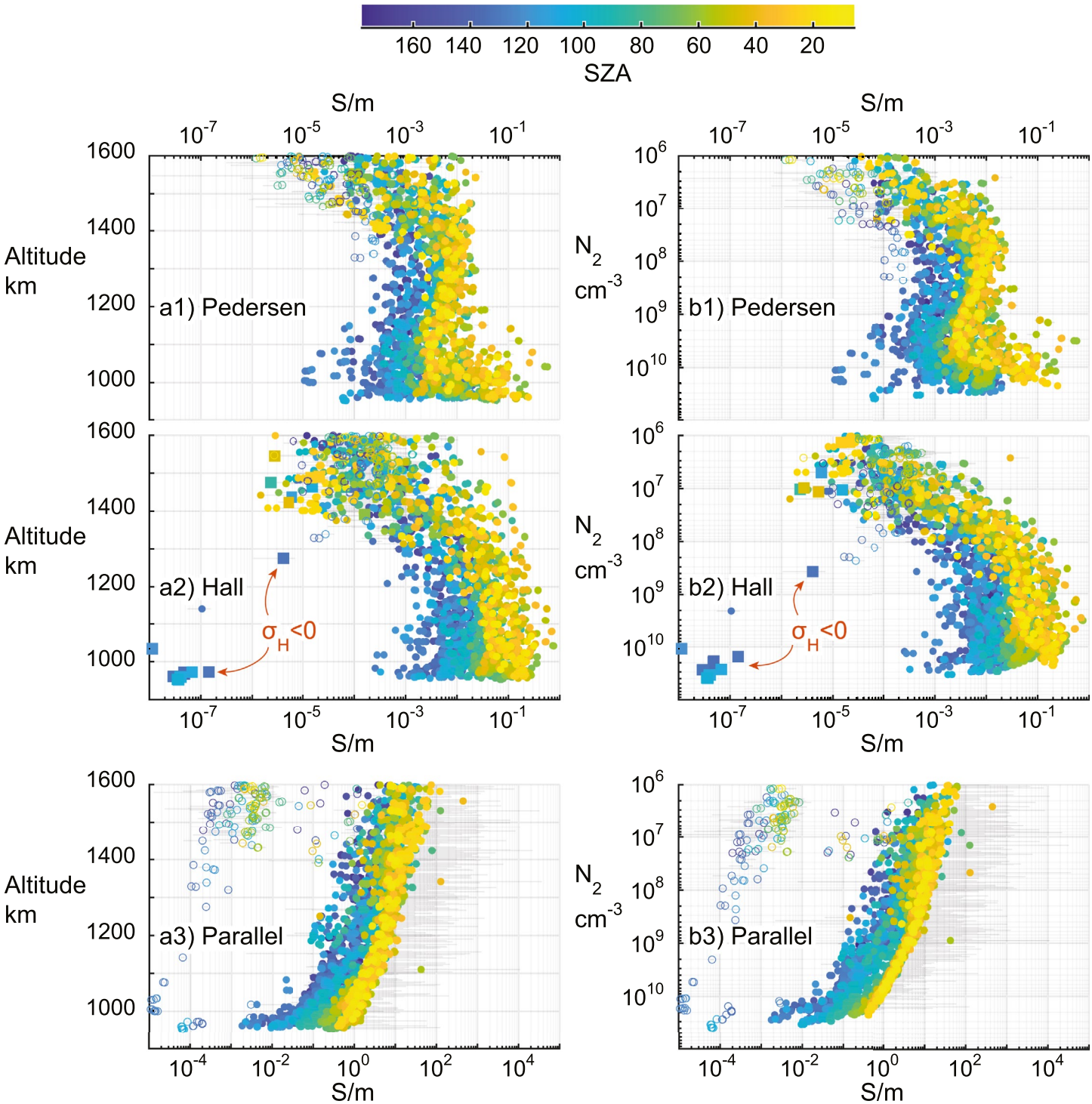

Figure 3. Titan's ionospheric conductivities: Pedersen (panels a1, b1), Hall (a2, b2) and Parallel (a3, b3), plotted in altitude (left-side panels a1–a3) and the measured N_2 densities (right-side panels b1–b3). The solar zenith angle is color-coded. Red arrows mark negative Hall conudctivities (reverse Hall effect).

due to a reduced recombination rate since electrons are depleted (Vigren et al., 2014), scaling the conductivities accordingly. A higher σ_P would mean that proportionally weaker electric field is required to drive a given Pedersen current. Unfortunately, there was no DC electric field instrument on Cassini, so another possibility is that for a given electric field, higher conductivity would mean proportionally larger current. A more conductive ionosphere will also more effectively shield out the ambient magnetic field, it is therefore possible that the sharp

drop of the magnetic field near the CA is a consequence of the σ_P enhancement in dusty plasma. In such a case, the highly conductive dusty plasma on Titan is a double-edged sword: on one hand, it is easier for currents to flow, on the other hand, the ambient magnetic field is shielded out and cannot induce the electric field to drive the currents. More on this below.

Comparing the altitude profiles (Figure 3 panels a1–a3) to the profiles versus measured neutral densities (panels b1–b3), the latter are more structured. Evidently, some of the variability below 1,100 km altitudes can be attributed to the variabilities of the neutral atmosphere. In particular, the increase of the Pedersen conductivity below 1,100 km altitude is less smeared vertically: the nightside values at ~1,000 km altitude correspond to N_2 densities of $\sim 5 \times 10^9$ cm^{-3} while the dayside values at same altitude correspond to N_2 densities of $\sim 10^{10}$ cm^{-3}.

Of note is a group of data points that stands out from the data set for all three conductivities in Figure 3, these correspond to flybys during solar maximum and have enhanced plasma densities (Edberg et al., 2013b; Shebanits et al., 2017), among which one (T85) also coincided with Titan excursion to Saturn's magnetosheath (Edberg et al., 2013a).

3.3. Dusty Plasma Influence

The sharp increase in σ_P near CA has been attributed to the decrease of the magnetic field strength (Rosenqvist et al., 2009), pre-dating the discovery of the negative ions/dust grains in the RPWS data (Ågren et al., 2012; Shebanits et al., 2013). Interestingly, although the increase of σ_P does coincide with an increase in positive ion and negative ion/dust densities, the main influence is indeed the decrease in the magnetic field. This is evident in Figure 4 which shows σ_P (left panels a1, a2) and σ_H (right panels b1, b2) below 1,200 km altitude plotted versus magnetic field strength $|B|$, dayside points in top panels (a1, b1) and nightside points in bottom panels (a2, b2). On the nightside, an impact of $|B|$ is much more difficult to discern for both σ_P and σ_H, owing to larger ionospheric variability compared to the dayside. However, one should keep in mind that the decrease in $|B|$ may be caused by the dusty plasma as mentioned above. It is also worth mentioning that the trend in $|B|$ persists regardless of the nominal corotational plasma ram direction.

As mentioned above, the presence of dusty plasma strongly diminishes or even reverses σ_H. In Titan's ionosphere, a low electron depletion ratio n_e/n_i has been demonstrated to be a sufficient indicator for a dusty plasma (Shebanits et al., 2016). In Figure 4, the electron depletion ratio is colorcoded (dark = dusty) and the n_e/n_i trend in σ_H is clearly visible for the nightside ionosphere (panel b2). On the dayside the plasma is less dusty (lower n_e/n_i) at the CA compared to the nightside, consequently the trend is weaker (panel b1) but expected to manifest at lower altitudes as the dusty plasma is a global phenomenon in Titan's ionosphere (Shebanits et al., 2016). This introduces a layer of complexity to the ionospheric current system that is unique to Titan so far. The trend in σ_P is less obvious (panels a1, a2) but the "dustier" plasma generally corresponds to larger values. In particular, $\sigma_P \approx \sigma_\parallel$ in the most dusty cases near CA (nightside where $\sigma_H < 0$), and since the peak of the dusty plasma is below the CA (Shebanits et al., 2017) $\sigma_\parallel$ may not represent the total ionospheric conductivity at lower altitudes as was suggested by (Rosenqvist et al., 2009).

3.4. General Picture

Median profiles of the conductivities from Figure 3 are shown in Figure 5 versus the measured N_2 densities (panels a1–a3) and versus altitude (panels b1–b3), colorcoded into dayside ($SZA < 70$, orange), terminator ($70 \leq \mathrm{SZA} < 100$, green) and nightside ($\mathrm{SZA} \geq 100$, blue) regions. Notably, σ_P peaks plotted in altitude (panel b1) appear slightly broader on the dayside and terminator than on the nightside. From comparison of the altitude profile altitude in panel b1 to those plotted versus the measured neutral densities in panel a1, this seems to be either an effect of the neutral atmosphere shifting in altitude between day and night, or ionosphere exhibiting larger variability on the dayside. As mentioned above, the differences in the dayside, terminator and nightside profiles follow the respective positive ion density profiles (electrons for field-parallel conductivity). This is also reflected in the top σ_P peaks, which are wider on the dayside and become narrower towards the nightside as well as tending towards higher altitudes, to be compared with the peaks of ion densities increasing in altitude towards the nightside (Shebanits et al., 2017) and a similar trend in the peaks of electron densities (Ågren et al., 2009). The total median profiles are shown in black and follow the terminator profiles quite closely because Titan's extensive atmosphere creates a smooth day to night transition.

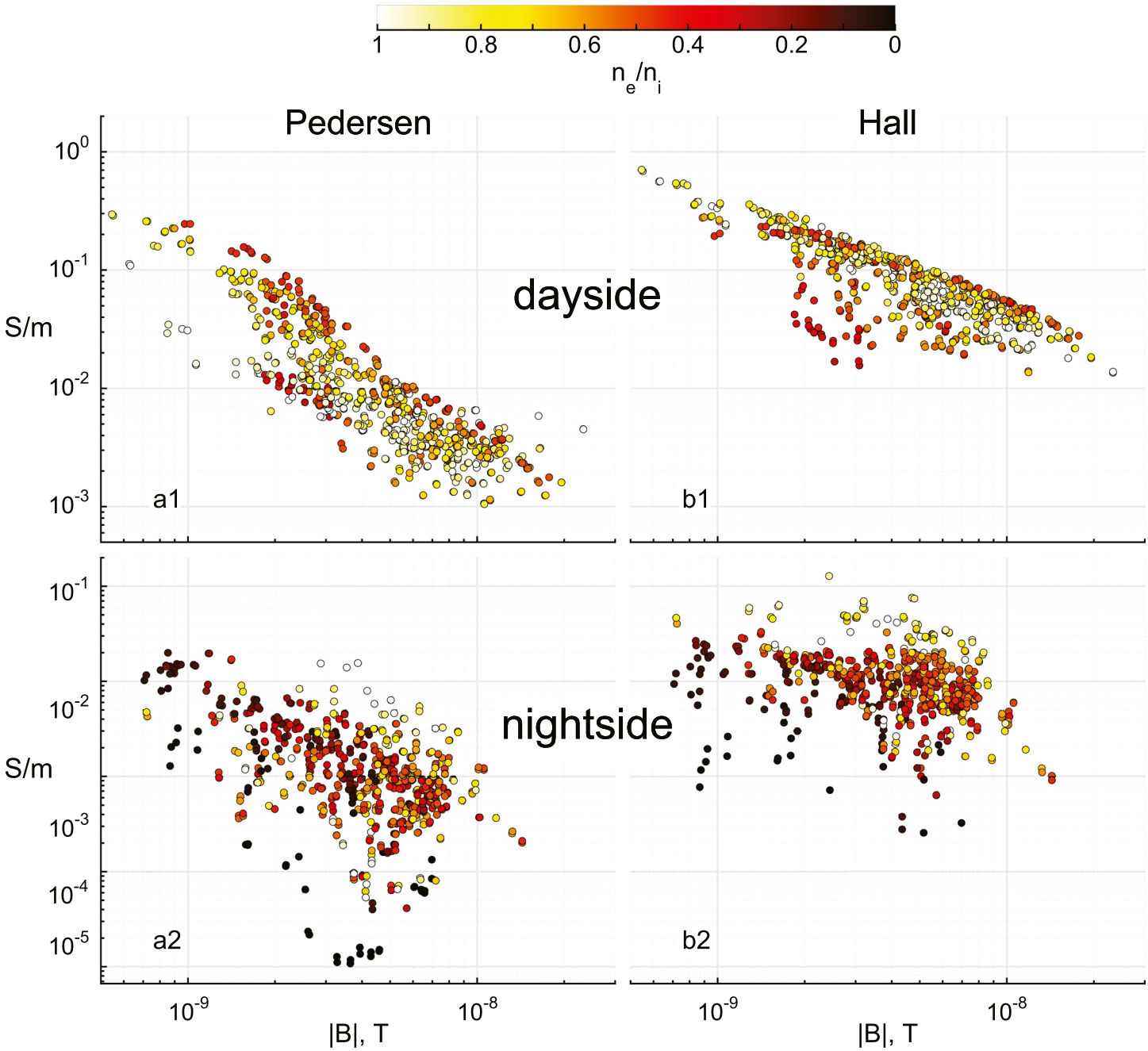

Figure 4. Pedersen (left panels a1, a2) and Hall (right panels b1, b2) conductivities below 1,200 km plotted versus magnetic field strength $|B|$. The electron depletion ratio n_e/n_i (color-coded) indicates the regions of dusty plasma. Top panels a1, b1 show dayside ionosphere (SZA < 90°), bottom panels a2, b2 show nightside (SZA > 90°).

Solar cycle has been shown to modulate Titan's ionosphere (Edberg et al., 2013b; Shebanits et al., 2017) and atmosphere (Westlake et al., 2014). Since the conductivities scale approximately linearly with the plasma densities, the same effect on the conductivities is anticipated. We plot in Figure 6 medians of solar minimum (faint lines, EUV flux < 26.5 μWm^{-2}) and solar maximum (solid lines, EUV flux > 26.5 μWm^{-2}) for dayside (yellow) and nightside (blue) ionosphere. Comparing the altitude profiles in panels b1–b3 to the profiles plotted versus neutral atmosphere in panels a1–a3 it is evident that the differences above 1,100 km are due to the vertical shift in the background neutral densities. Below ~1,100 km (~ 10^9 cm^{-3} N_2) the profiles diverge (especially on the nightside) following the change in the charge densities of the heavy charge carriers presented in Shebanits

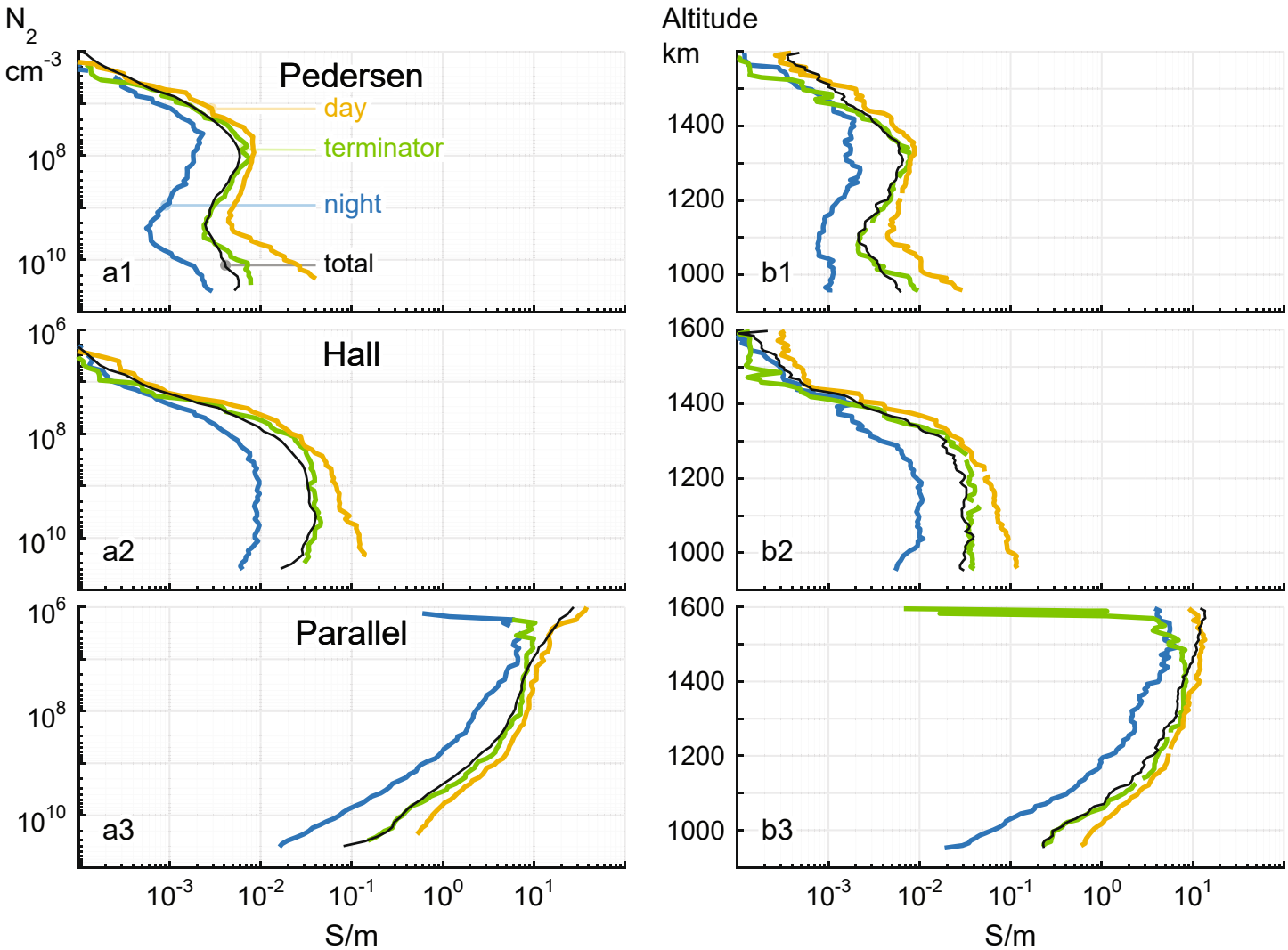

Figure 5. General conductivity profiles for all included flybys: Pedersen (panels a1, b1), Hall (panels a2, b2) and Parallel (panels a3, b3). The total medians are in solid black. The colored lines are medians for the **dayside (orange, SZA < 70), terminator (green, 70 ≤ SZA > 100) and nightside (blue,** SZA ≥ **100).** All profiles are sliding medians over binned N2 densities (panels a1–a3) and altitudes (panels b1–b3).

et al., 2017–an increase on the dayside and a decrease on the nightside between solar minimum and maximum. The effect is most pronounced for the Pedersen conductivities (mostly governed by the positive ions and negative ions/dust grains) and least pronounced for the field-parallel conductivities (mostly governed by electrons). This figure further accentuates the importance of using the neutral atmosphere as a vertical coordinate.

The impact of charged dust is shown in Figure 7: panels a1–a3 show median ratios of the conductivities derived with only electron densities, $\sigma(n_e)$, to the conductivities derived with full plasma content, $\sigma(n_e, n_i, n_d)$, with the same color-coding as in Figure 5. Faded lines show electron depletion ratio (n_e/n_i) for reference, plotted in panel a2. First thing to note is that the ratios of σ_P and σ_H deviate from 1 above ~1,400 km altitude (outside the dynamo region) due to minor peaks in the positive ion densities (Shebanits et al., 2017), possibly caused by plasma transport (Ågren et al., 2009; Cravens et al., 2009; Cui et al., 2010).

It is evident that already for $n_e/n_i < 0.9$ the Pedersen conductivity $\sigma_P(n_e)$ is typically underestimated (median of $\sigma(n_e)/\sigma(n_e, n_i, n_d) < 1$), especially on the nightside (by up to 35%), while for σ_H and $\sigma_\parallel$ there is virtually no impact. Because the already weak external magnetic field diminishes near CA, the σ_P ratio increases below ~1,100 km altitude to 0.99 for dayside and terminator and to 0.92 on the nightside. This means that the electron contributions become dominant again, although somewhat less so on the night side where, $n_e/n_i < 0.4$. This does

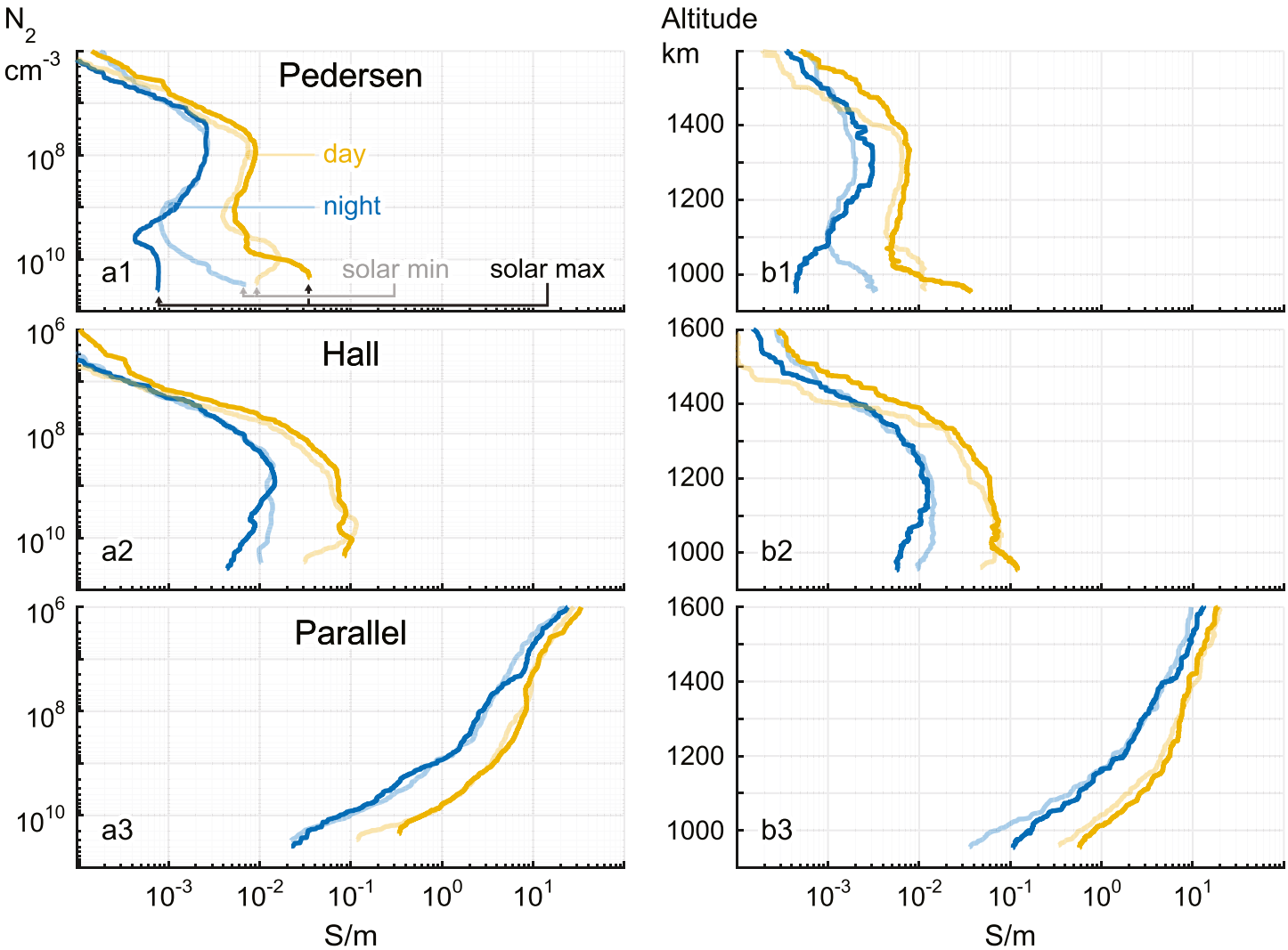

Figure 6. Medians of conductivities during solar minimum (faint lines, EUV flux < 26.5 μWm^{-2}) and solar maximum (solid lines, EUV flux > 26.5 μWm^{-2}) for dayside (yellow) and nightside (blue) ionosphere. The same sliding median is applied as in Figure 5.

not mean that the second σ_P peak below CA will not be affected by the dusty plasma but rather that the expression of this effect is entirely dependent on whether the magnetic field is strong enough.

An important caveat. The ratio in Figure 7 panels a1–a3 compares conductivities derived with the full plasma content to those derived with the electron densities alone, but these electron densities are still *measured in a dusty plasma*. It therefore demonstrates that relying on electron densities alone in a dusty plasma leads to underestimates of the plasma conductivities, even in Titan's case of absent internal magnetic field, but it does not indicate what the conductivities would be if Titan's ionosphere was dust-free.

Comparison with the previous conductivity study (Rosenqvist et al., 2009 below "R2009" for short) is shown in Figure 7 panels b1–b3, where their median profiles are plotted in red (17 flybys, marked 17 R2009). The other profiles are derived using the data set from the current work, matching the same 17 flybys: medians using only electron densities (same method as R2009) are shown in dashed blue lines marked 17 w/o dust and medians with full plasma content (including dust) as gray lines marked 17 w dust. The original R2009 data set is unfortunately not available and some of the key parameters have since been updated. Specifically, R2009 used neutral densities from a model by Müller-Wodarg et al. (2008), a constant electron temperature of 0.1 eV (1160 K) and a single positive ion population (28 amu). The neutral densities have been shown to vary in altitude with solar activity (Westlake et al., 2014) and the INMS data set has also been re-calibrated (Teolis et al., 2015). Typical electron

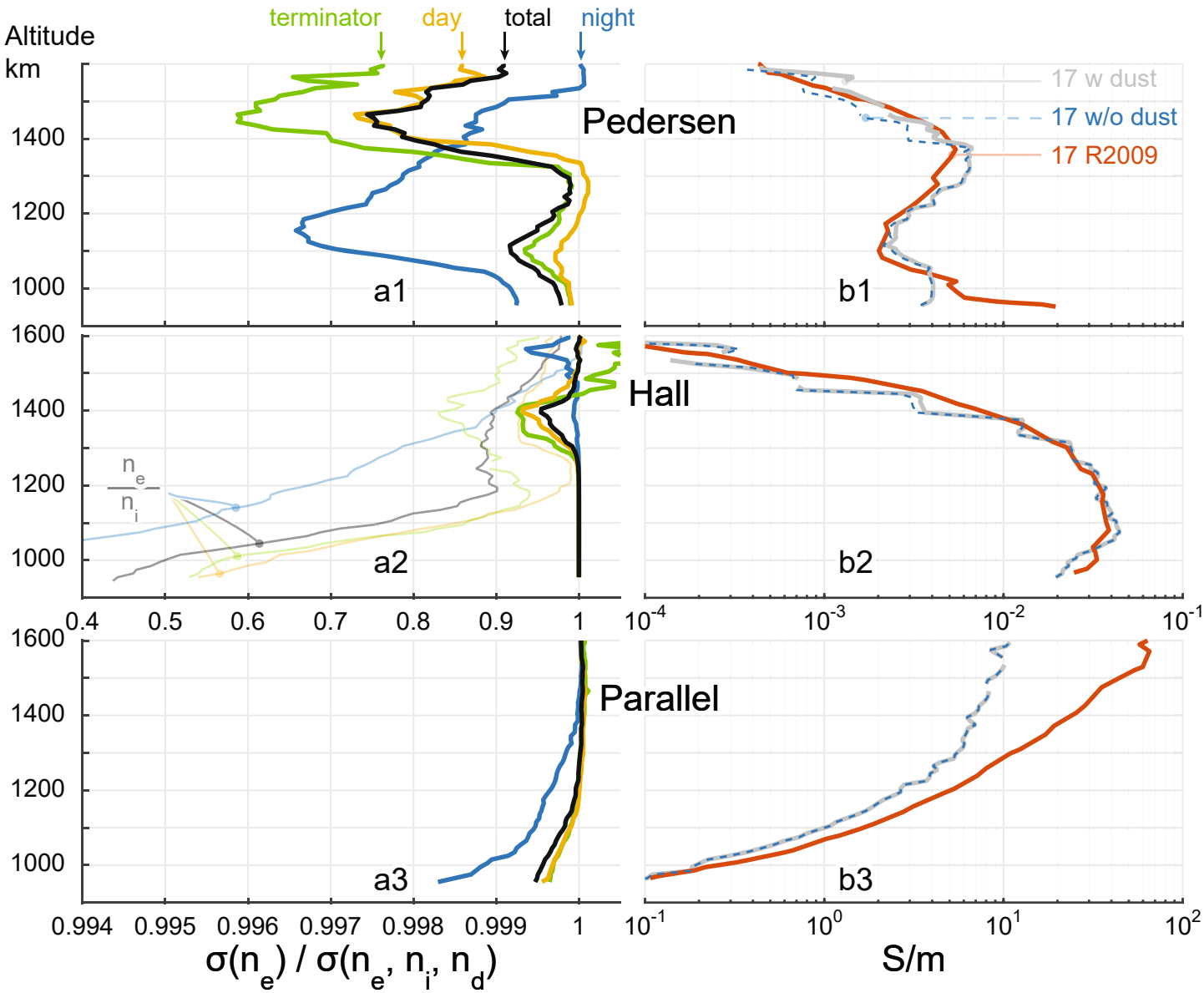

Figure 7. Left side panels a1–a3 show day (orange)/terminator (green)/night (blue) and total ratios of the Pedersen (a1), Hall (a2) and Parallel (a3) conductivities derived without dust $\sigma(n_e)$ and with dust $\sigma(n_e, n_i, n_d)$. Note the different scale of the panel a3 x-axis. The electron depletion ratios n_e/n_i (same color scheme) are plotted for reference as fainter lines in panel a2. All profiles in panels a1–a3 are sliding medians binned in altitudes in the same way as in Figure 5. Right side panels b1–3 show comparison with the Rosenqvist et al. (2009) medians (red lines marked 17 R2009). Gray lines marked 17 w dust shows the same 17 flybys as 17 R2009 but with dust included. Blue lines marked 17 w/o dust are same as gray profiles but derived using electron densities only.

temperatures below 1,100 km altitude are 0.026–0.052 eV (300–600 K; Edberg et al., 2010). The mean positive ion mass increases exponentially towards lower altitudes and reaches ~120 amu near CA (Shebanits et al., 2016). The latter seems to be responsible for the divergence of the red and dashed blue profiles near CA. Despite this, we can conclude that the R2009 profiles and the current work are generally consistent. For the impact of the dusty plasma, the difference between the dashed blue and gray profiles in Figure 7 (panels b1–b3) follows the median of the total ratio in panels a1–a3 (black line).

Comparing Titan's dusty ionosphere with that of Saturn, the impact of charged dust on the conductivities is very different. On Saturn, the Pedersen conductivities were increased by up to two orders of magnitude and the Hall conductivities reduced or reversed already above the upper peak of ionospheric plasma densities (Shebanits et al., 2020). On Titan, the impact of the dusty plasma becomes prominent only below the first ionospheric

peak (~1,100–1,200 km), with signs of the reverse Hall effect mostly near the CA. This is because the sources of the dust grains are different. On Saturn, the dust grains fall in from the D-ring (Hamil et al., 2018; e.g., Hsu et al., 2018; Mitchell et al., 2018) in addition to possibly forming in the top ionosphere (Waite et al., 2018), and are already present in significant quantities in the top ionosphere (Morooka et al., 2019), well above the main photoionization peak (Hadid et al., 2018). On Titan, the dust grains are chemically formed in the ionosphere itself (Desai et al., 2017; Lavvas et al., 2013; Vuitton et al., 2009; Waite et al., 2007) and reach densities comparable to electrons and positive ions well below the photoionization peak. The impact of dusty plasma also generally diminishes with decreasing magnetic field strength near CA, because Titan does not have an internal magnetic field and the external magnetic field is four magnitudes smaller than in Saturn's ionosphere.

4. Summary and Conclusions

We calculate the electric conductivities of Titan's ionosphere using the in-situ data set from the entire Cassini mission (58 flybys). Full ionospheric plasma content (electrons, positive ions and negative ions/dust grains) is utilized. Our observations show the following:

1. The Pedersen conductivities in Titan's nightside ionosphere between ~1,100 and 1,400 km altitudes have up to 35% contributions from the heavy charge carriers (3%–7% on dayside/terminator). This means that using electron densities alone will underestimate the Pedersen conductivity accordingly. In particular, the conductivities derived here are expected to increase the previous estimates of the ionospheric currents (Ågren et al., 2011).
2. The Hall and field-parallel conductivities are virtually unaffected by the dusty plasma due to a weak external magnetic field that further decreases near CA–in contrast to ionospheres of bodies with internal magnetic field.
3. The bulk of Titan's ionosphere in the 1,000–1,400 km altitude range is dominated by the Hall conductivity. Subsequently, Hall currents are expected to be the dominant horizontal currents in this region, a typical scenario in planetary ionospheres as the Pedersen currents interface between the ionospheric Hall currents and the magnetospheric field-parallel currents.
4. The difference between the dayside and nightside conductivities is about an order of magnitude with terminator conductivities roughly in-between.
5. Previously reported solar cycle effects on the ionospheric densities propagate to conductivities, with most prominent differences below ~1,100 km altitude: Pedersen and Hall conductivities during solar maximum are higher on the dayside but lower on the nightside (compared to solar minimum).
6. The sharp increase of the Pedersen conductivity below 1,100 km altitude coincides with the dusty region of Titan's ionosphere, suggesting a dusty plasma layer dominated by the Pedersen conductivity (and subsequently, Pedersen currents). The main cause of this increase is a decreasing magnetic field. On one hand, a necessary condition for such second Pedersen layer to form is a magnetic field strong enough to magnetize the electrons. On the other hand, the dusty plasma densities are much higher than the first ionospheric peak and will act to shield out the external magnetic field. This is speculative however, as there are no magnetic field measurements below CA and modeling efforts will be required to draw definitive conclusions.
7. The Hall conductivity shows indications of a reverse Hall effect at ~950 km altitude. Although the reversed Hall conductivities are much smaller than the Pedersen conductivities in the same region, they will change the direction of Hall currents which affects the overall configuration of the ionospheric current system.

A similar double-peak behavior of Pedersen conductivities was found in Martian ionosphere (Opgenoorth et al., 2010), where dust may be introduced into the plasma by meteorites and dust storms (e.g., Crismani et al., 2018; Felici et al., 2020). These results are therefore relevant for unmagnetized planetary bodies with draped magnetic field and possible ionospheric dust/aerosol presence, like Venus and Mars as well as moons of giant planets.

Appendix A: Average Mass and Dust Charge Effects

A validation of using the total densities and average masses of the heavy plasma species is performed for the dayside case T40, terminator case of T16 and nightside cases of T29 and T56 (Figure A1 panels a1–a4), where the mass spectra are available simultaneously for the positive ions (Shebanits et al., 2016) and negative ions/dust

grains (Coates et al., 2009, 2010; Shebanits et al., 2016). The solid lines represent the average Pedersen (blue), Hall (red) and magnetic field parallel (yellow) conductivity profiles, all in a very good agreement with the respective conductivities derived using the full mass spectra (square markers). The corresponding plasma charge densities are shown for reference (panels b1–b4). During T16 and T56 the electrons were sufficiently depleted for the Hall conductivity to become slightly negative (as indicated in panels a1 and a4).

One of the parameters associated with the size and shape of the grains is the charge. Empirical estimate of the average dust grain charge suggests values between −1.5 and −2.5 for these flybys (Shebanits et al., 2016), while theoretical predictions (for spherical grains) suggest most likely charge to be $Z_d = -1$ (Draine & Sutin, 1987; Meyer-Vernet, 2013). The impact of the grain charge can be seen in Figure A1 panels a1–a4, where the singly charged grains are used for the solid lines and the empirically estimated Z_d is used for the dashed lines. The difference between these cases is <5% for T40 and <10% for T29 and T56, approximately a third of the combined measurement uncertainties. For this reason, the conductivities for all flybys are derived assuming $Z_d = -1$.

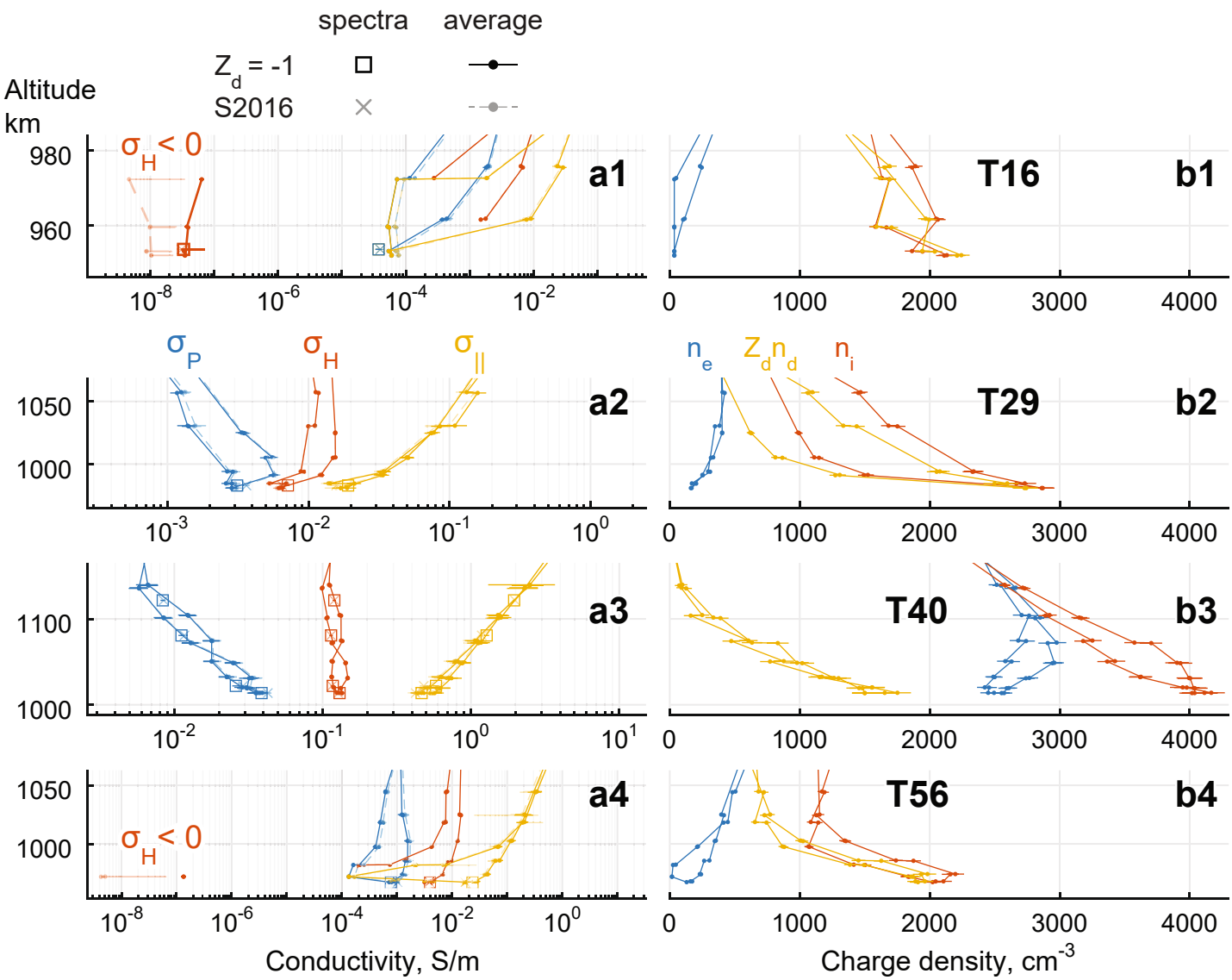

Figure A1. Panels a1–4: Comparison of the T16, T29, T40 and T56 conductivities derived using the average plasma species masses (solid lines with dot markers) and using the full mass spectra (squares and crosses) of the positive ions and negative ions/dust. Squares and solid lines are derived assuming singly charged particles, fainter crosses and dashed lines are derived using the empirical average negative ion and dust grain charge estimate. Panels b1–b4: the corresponding plasma densities, for reference. The CAPS IBS mass spectra, dust charge estimate and densities datasets are from Shebanits et al., 2016. The CAPS ELS mass spectra are from Coates et al., 2009, 2010, and Shebanits et al., 2016.

It should be noted that the corresponding difference between the full mass spectra data points (squares and crosses) for T29 and T56 is larger (∼15% and ∼25% respectively). This is because the average dust charge estimate is applied to the entire mass spectrum–in reality, only the heavier (larger) grains are likely to hold more than a single charge and these datapoints should be considered as extreme examples in absence of a detailed grain charging model. See also discussion in Shebanits et al., 2016 (their Section 4.3).

Data Availability Statement

The data set used in the current study are available in a Mendeley Data repository, https://data.mendeley.com/datasets/hwc5wfbvj9/1.

Acknowledgments
O. Shebanits acknowledges funding by SNSA Dnr 195/20. J.-E. Wahlund acknowledges the support of the Cassini RPWS/LP operations by SNSA. J. H. Waite worked under internal funding from the Division of Space Science and Engineering, Southwest Research Institute. M. K. Dougherty acknowledges funding by Royal Society Research Professorship RP140004.

References

Ågren, K., Andrews, D. J., Buchert, S. C., Coates, A. J., Cowley, S. W. H., Dougherty, M. K., et al. (2011). Detection of currents and associated electric fields in Titan's ionosphere from Cassini data. *Journal of Geophysical Research: Space Physics*, *116*(A4). https://doi.org/10.1029/2010ja016100

Ågren, K., Edberg, N. J. T., & Wahlund, J. E. (2012). Detection of negative ions in the deep ionosphere of Titan during the Cassini T70 flyby. *Geophysical Research Letters*, *39*, L10201. https://doi.org/10.1029/2012GL051714

Ågren, K., Wahlund, J.-E., Garnier, P., Modolo, R., Cui, J., Galand, M., & Müller-Wodarg, I. (2009). On the ionospheric structure of Titan. *Planetary and Space Science*, 57. https://doi.org/10.1016/j.pss.2009.04.012

Bertucci, C., Achilleos, N., Dougherty, M. K., Modolo, R., Coates, A. J., Szego, K., et al. (2008). The magnetic memory of Titan's ionized atmosphere. *Science*, *321*. https://doi.org/10.1126/science.1159780

Bertucci, C., Duru, F., Edberg, N., Fraenz, M., Martinecz, C., Szego, K., & Vaisberg, O. (2011). The induced magnetospheres of Mars, Venus, and Titan. *Space Science Reviews*, *162*. https://doi.org/10.1007/s11214-011-9845-1

Brouet, Y., Levasseur-Regourd, A. C., Sabouroux, P., Neves, L., Encrenaz, P., Poch, O., et al. (2016). A porosity gradient in 67P/C-G nucleus suggested from CONSERT and SESAME-PP results: An interpretation based on new laboratory permittivity measurements of porous icy analogues. *Monthly Notices of the Royal Astronomical Society*, *462*. https://doi.org/10.1093/mnras/stw2151

Chatain, A., Carrasco, N., Ruscassier, N., Gautier, T., Vettier, L., & Guaitella, O. (2020). Interaction dust–Plasma in Titan's ionosphere: An experimental simulation of aerosols erosion. *Icarus*, *345*, 113741. https://doi.org/10.1016/j.icarus.2020.113741

Chatain, A., Wahlund, J. E., Shebanits, O., Hadid, L. Z., Morooka, M., Edberg, N. J. T., et al. (2021a). Re-analysis of the Cassini RPWS/LP data in Titan's ionosphere: 1. Detection of several electron populations. *Journal of Geophysical Research: Space Physics*, *126*, e2020JA028412. https://doi.org/10.1029/2020JA028412

Chatain, A., Wahlund, J. E., Shebanits, O., Hadid, L. Z., Morooka, M., Edberg, N. J. T., et al. (2021b). Re-analysis of the Cassini RPWS/LP data in Titan's ionosphere: 2. Statistics on 57 flybys. *Journal of Geophysical Research: Space Physics*, *126*, e2020JA028413. https://doi.org/10.1029/2020JA028413

Coates, A. J., Crary, F. J., Lewis, G. R., Young, D. T., Waite, J. H., & Sittler, E. C. (2007). Discovery of heavy negative ions in Titan's ionosphere. *Geophysical Research Letters*, *34*(22). https://doi.org/10.1029/2007gl030978

Coates, A. J., Wellbrock, A., Lewis, G. R., Jones, G. H., Young, D. T., Crary, F. J., & Waite, J. H. (2009). Heavy negative ions in Titan's ionosphere: Altitude and latitude dependence. *Planetary and Space Science*, *57*(14–15), 1866–1871. https://doi.org/10.1016/j.pss.2009.05.009

Coates, A. J., Wellbrock, A., Lewis, G. R., Jones, G. H., Young, D. T., Crary, F. J., et al. (2010). Negative ions at Titan and Enceladus: Recent results. *Faraday Discussions*, *147*. https://doi.org/10.1039/c004700g

Cravens, T., Robertson, I., Waitejr, J., Yelle, R., Vuitton, V., Coates, A., et al. (2009). Model-data comparisons for Titan's nightside ionosphere. *Icarus*, *199*(1), 174–188. https://doi.org/10.1016/j.icarus.2008.09.005

Crismani, M. M. J., Schneider, N. M., Evans, J. S., Plane, J. M. C., Carrillo-Sánchez, J. D., Deighan, J., & Yelle, R. (2018). The impact of comet Siding Spring's meteors on the Martian atmosphere and ionosphere. *Journal of Geophysical Research: Planets*, *123*(10), 2613–2627. https://doi.org/10.1029/2018je005750

Cui, J., Galand, M., Yelle, R. V., Wahlund, J. E., Ågren, K., Waite, J. H., & Dougherty, M. K. (2010). Ion transport in Titan's upper atmosphere. *Journal of Geophysical Research: Space Physics*, *115*(A6). https://doi.org/10.1029/2009ja014563

Desai, R. T., Coates, A. J., Wellbrock, A., Vuitton, V., Crary, F. J., González-Caniulef, D., et al. (2017). Carbon chain anions and the growth of complex organic molecules in Titan's ionosphere. *The Astrophysical Journal*. https://doi.org/10.3847/2041-8213/aa7851

Dougherty, M. K., Kellock, S., Southwood, D. J., Balogh, A., Smith, E. J., Tsurutani, B. T., et al. (2004). The Cassini magnetic field investigation. *Space Science Reviews*, *114*. https://doi.org/10.1007/s11214-004-1432-2

Draine, B. T., & Sutin, B. (1987). Collisional charging of interstellar grains. *The Astrophysical Journal*, *320*. https://doi.org/10.1086/165596

Edberg, N. J. T., Andrews, D. J., Shebanits, O., Ågren, K., Wahlund, J. E., Opgenoorth, H. J., et al. (2013a). Extreme densities in Titan's ionosphere during the T85 magnetosheath encounter. *Geophysical Research Letters*, *40*(12), 2879–2883. https://doi.org/10.1002/grl.50579

Edberg, N. J. T., Andrews, D. J., Shebanits, O., Ågren, K., Wahlund, J. E., Opgenoorth, H. J., et al. (2013b). Solar cycle modulation of Titan's ionosphere. *Journal of Geophysical Research: Space Physics*, *118*(8), 5255–5264. https://doi.org/10.1002/jgra.50463

Edberg, N. J. T., Vigren, E., Snowden, D., Regoli, L. H., Shebanits, O., Wahlund, J. E., et al. (2018). Titan's variable ionosphere during the T118 and T119 Cassini flybys. *Geophysical Research Letters*, *45*(17), 8721–8728. https://doi.org/10.1029/2018gl078436

Edberg, N. J. T., Wahlund, J.-E., Ågren, K., Morooka, M. W., Modolo, R., Bertucci, C., & Dougherty, M. K. (2010). Electron density and temperature measurements in the cold plasma environment of Titan: Implications for atmospheric escape. *Geophysical Research Letters*, *37*, L20105. https://doi.org/10.1029/2010GL044544

Felici, M., Withers, P., Smith, M. D., González-Galindo, F., Oudrhiri, K., & Kahan, D. (2020). MAVEN Observations of the response of the martian ionosphere to dust storms. *Journal of Geophysical Research: Space Physics*, *125*, e2019JA027083. https://doi.org/10.1029/2019JA027083

Garnier, P., Dandouras, I., Toublanc, D., Roelof, E. C., Brandt, P. C., Mitchell, D. G., et al. (2010). Statistical analysis of the energetic ion and ENA data for the Titan environment. *Planetary and Space Science*, *58*(14–15), 1811–1822. https://doi.org/10.1016/j.pss.2010.08.009

Gurnett, D. A., Kurth, W. S., Kirchner, D. L., Hospodarsky, G. B., Averkamp, T. F., Zarka, P., et al. (2004). The Cassini radio and plasma wave investigation. *Space Science Reviews*, *114*(1–4), 395–463. https://doi.org/10.1007/s11214-004-1434-0

Hadid, L. Z., Morooka, M. W., Wahlund, J. E., Persoon, A. M., Andrews, D. J., Shebanits, O., et al. (2018). Saturn's ionosphere: Electron density altitude profiles and D-Ring interaction from The Cassini grand finale. *Geophysical Research Letters*, *46*, 9362–9369. https://doi.org/10.1029/2018GL078004

Hamil, O., Cravens, T. E., Reedy, N. L., & Sakai, S. (2018). Fate of ice grains in Saturn's ionosphere. *Journal of Geophysical Research: Space Physics*, *123*(2), 1429–1440. https://doi.org/10.1002/2017ja024616

Hsu, H.-W., Schmidt, J., Kempf, S., Postberg, F., Moragas-Klostermeyer, G., Seiß, M., et al. (2018). In situ collection of dust grains falling from Saturn's rings into its atmosphere. *Science*, *362*. https://doi.org/10.1126/science.aat3185

Imanaka, H., Cruikshank, D. P., Khare, B. N., & McKay, C. P. (2012). Optical constants of Titan tholins at mid-infrared wavelengths (2.5–25μm) and the possible chemical nature of Titan's haze particles. *Icarus*, *218*. doi https://doi.org/10.1016/j.icarus.2011.11.018

Itikawa, Y. (2006). Cross sections for electron collisions with nitrogen molecules, *Journal of Physical and Chemical Reference Data*, *35*. https://doi.org/10.1063/1.1937426

Lavvas, P., Yelle, R. V., Koskinen, T., Bazin, A., Vuitton, V., Vigren, E., et al. (2013). Aerosol growth in Titan's ionosphere. *Proceedings of the National Academy of Sciences*, *110*. https://doi.org/10.1073/pnas.1217059110

Lellouch, E., Gurwell, M. A., Moreno, R., Vinatier, S., Strobel, D. F., Moullet, A., et al. (2019). An intense thermospheric jet on Titan. *Nature Astronomy*, *3*. https://doi.org/10.1038/s41550-019-0749-4

Meyer-Vernet, N. (2013). On the charge of nanograins in cold environments and Enceladus dust. *Icarus*, *226*. https://doi.org/10.1016/j.icarus.2013.06.014

Michael, M., Tripathi, S. N., Arya, P., Coates, A., Wellbrock, A., & Young, D. T. (2011). High-altitude charged aerosols in the atmosphere of Titan. *Planetary and Space Science*, *59*. https://doi.org/10.1016/j.pss.2011.03.010

Mitchell, D. G., Perry, M. E., Hamilton, D. C., Westlake, J. H., Kollmann, P., Smith, H. T., et al. (2018). Dust grains fall from Saturn's D-ring into its equatorial upper atmosphere. *Science*, *362*. https://doi.org/10.1126/science.aat2236

Morooka, M. W., Wahlund, J.-E., Eriksson, A. I., Farrell, W. M., Gurnett, D. A., Kurth, W. S., et al. (2011). Dusty plasma in the vicinity of Enceladus. *Journal of Geophysical Research: Space Physics*, *116*(A12). https://doi.org/10.1029/2011ja017038

Morooka, M. W., Wahlund, J.-E., Hadid, L. Z., Eriksson, A. I., Edberg, N. J. T., Vigren, E., et al. (2019). Saturn's dusty ionosphere, *Journal of Geophysical Research: Space Physics*, *124*, 1679–1697. https://doi.org/10.1029/2018JA026154

Müller-Wodarg, I. C. F., Yelle, R. V., Cui, J., & Waite, J. H. (2008). Horizontal structures and dynamics of Titan's thermosphere. *Journal of Geophysical Research*, *113*(E10). https://doi.org/10.1029/2007je003033

Muralikrishna, P., & Kulkarni, V. H. (2006). On the height variation of the E-region cowling conductivity–effect of charged dust particles. *Annales Geophysicae*, *24*(11), 2949–2957. https://doi.org/10.5194/angeo-24-2949-2006

Niemann, H. B., Atreya, S. K., Bauer, S. J., Carignan, G. R., Demick, J. E., Frost, R. L., et al. (2005). The abundances of constituents of Titan's atmosphere from the GCMS instrument on the Huygens probe. *Nature*, *438*. https://doi.org/10.1038/nature04122

Opgenoorth, H. J., Dhillon, R. S., Rosenqvist, L., Lester, M., Edberg, N. J. T., Milan, S. E., et al. (2010). Day-side ionospheric conductivities at Mars. *Planetary and Space Science*, *58*(10), 1139–1151. https://doi.org/10.1016/j.pss.2010.04.004

Rosenqvist, L., Wahlund, J.-E., Ågren, K., Modolo, R., Opgenoorth, H. J., Strobel, D., et al. (2009). Titan ionospheric conductivities from Cassini measurements. *Planetary and Space Science*, *57*(14–15), 1828–1833. https://doi.org/10.1016/j.pss.2009.01.007

Schunk, R., & Nagy, A. (2009). *Ionospheres* (2nd ed.). Cambridge University Press. http://ebooks.cambridge.org/ref/id/CBO9780511635342

Shebanits, O., Hadid, L. Z., Cao, H., Morooka, M. W., Hunt, G. J., Dougherty, M. K., et al. (2020). Saturn's near-equatorial ionospheric conductivities from in situ measurements. *Scientific Reports*, *101*. https://doi.org/10.1038/s41598-020-64787-7

Shebanits, O., Vigren, E., Wahlund, J. E., Holmberg, M. K. G., Morooka, M., Edberg, N. J. T., et al. (2017). Titan's ionosphere: A survey of solar EUV influences. *Journal of Geophysical Research: Space Physics*, 122, 7491–7503. https://doi.org/10.1002/2017JA023987

Shebanits, O., Wahlund, J.-E., Edberg, N. J. T., Crary, F. J., Wellbrock, A., Andrews, D. J., et al. (2016). Ion and aerosol precursor densities in Titan's ionosphere: A multi-instrument case study. *Journal of Geophysical Research: Space Physics*, *121*, 10075–10090. https://doi.org/10.1002/2016JA022980

Shebanits, O., Wahlund, J.-E., Mandt, K., Ågren, K., Edberg, N. J. T., & Waite, J. H. (2013). Negative ion densities in the ionosphere of Titan-Cassini RPWS/LP results. *Planetary and Space Science*, *84*, 153–162. https://doi.org/10.1016/j.pss.2013.05.021

Simon, S., Saur, J., Kriegel, H., Neubauer, F. M., Motschmann, U., & Dougherty, M. K. (2011). Influence of negatively charged plume grains and hemisphere coupling currents on the structure of Enceladus' Alfvén wings: Analytical modeling of Cassini magnetometer observations. *Journal of Geophysical Research: Space Physics*, *116*(A4). https://doi.org/10.1029/2010ja016338

Sittler, E. C., Ali, A., Cooper, J. F., Hartle, R. E., Johnson, R. E., Coates, A. J., & Young, D. T. (2009). Heavy ion formation in Titan's ionosphere: Magnetospheric introduction of free oxygen and a source of Titan's aerosols? *Planetary and Space Science*, *57*(13), 1547–1557. https://doi.org/10.1016/j.pss.2009.07.017

Song, M.-Y., Yoon, J.-S., Cho, H., Itikawa, Y., Karwasz, G. P., Kokoouline, V., et al. (2015). Cross sections for electron collisions with methane, *Journal of Physical and Chemical Reference Data*, *44*(2), 023101. https://doi.org/10.1063/1.4918630

Stankiewicz, A., Ionkina, N., Motherwell, B., Bennett, B., Wint, O., & Mastalerz, M. (2015). Kerogen density revisited–lessons from the Duvernay Shale. In *Proceedings of the 3rd Unconventional Resources Technology Conference*. American Association of Petroleum Geologists. https://library.seg.org/doi/abs/10.15530/urtec-2015-2157904

Teolis, B. D., Niemann, H. B., Waite, J. H., Gell, D. A., Perryman, R. S., Kasprzak, W. T., et al. (2015). A revised sensitivity model for Cassini INMS: Results at Titan. *Space Science Reviews*, *190*. https://doi.org/10.1007/s11214-014-0133-8

Vigren, E., Galand, M., Shebanits, O., Wahlund, J.-E., Geppert, W. D., Lavvas, P., et al. (2014). Increasing positive ion number densities below the peak of ion–electron pair production in titan's ionosphere. *The Astrophysical Journal*, *786*(1), 69. https://doi.org/10.1088/0004-637X/786/1/69

Vuitton, V., Lavvas, P., Yelle, R. V., Galand, M., Wellbrock, A., Lewis, G. R., et al. (2009). Negative ion chemistry in Titan's upper atmosphere. *Planetary and Space Science*, *57*(13), 1558–1572. https://doi.org/10.1016/j.pss.2009.04.004

Wahlund, J.-E. R., Boström, G., Gustafsson, D. A., Gurnett, W. S., Kurth, A., Pedersen, T. F., et al. (2005). Cassini measurements of cold plasma in the ionosphere of Titan. *Science*, 308. https://doi.org/10.1126/science.1109807

Waite, J. H., Lewis, W. S., Kasprzak, W. T., Anicich, V. G., Block, B. P., Cravens, T. E., et al. (2004). The Cassini ion and neutral mass spectrometer (INMS) investigation. *Space Science Reviews*, *114*. https://doi.org/10.1007/s11214-004-1408-2

Waite, J. H., Niemann, H., Yelle, R. V., Kasprzak, W. T., Cravens, T. E., Luhmann, J. G., et al. (2005). Ion neutral mass spectrometer results from the first flyby of Titan. *Science*, *308*. https://doi.org/10.1126/science.1110652

Waite, J. H., Perryman, R. S., Perry, M. E., Miller, K. E., Bell, J., Cravens, T. E., et al. (2018). Chemical interactions between Saturn's atmosphere and its rings. *Science*, *362*. https://doi.org/10.1126/science.aat2382

Waite, J. H., Young, D. T., Cravens, T. E., Coates, A. J., Crary, F. J., Magee, B., & Westlake, J. (2007). The process of tholin formation in Titan's upper atmosphere. *Science*, *316*. https://doi.org/10.1126/science.1139727

Waite, J. H., Young, D. T., Westlake, J. H., Lunine, J. I., McKay, C. P., & Lewis, W. S. (2009). High-altitude production of Titan's aerosols. *Titan from Cassini-Huygens* (201–204). Springer Netherlands. https://link.springer.com/10.1007/978-1-4020-9215-2_8

Westlake, J. H., Waite, J. H., Bell, J. M., & Perryman, R. (2014). Observed decline in Titan's thermospheric methane due to solar cycle drivers. *Journal of Geophysical Research: Space Physics*, *119*(10), 8586–8599. https://doi.org/10.1002/2014ja020394

Yaroshenko, V. V., & Lühr, H. (2016). Electrical conductivity of the dusty plasma in the Enceladus plume. *Icarus*, *278*, 79–87. https://doi.org/10.1016/j.icarus.2016.05.033